Chemical Engineering & Processing: Process Intensification 179 (2022) 109067

Contents lists available at ScienceDirect

Chemical Engineering and Processing - Process Intensification

journal homepage: www.elsevier.com/locate/cep

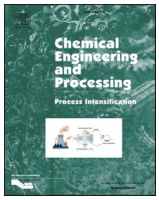

Physical and numerical characterisation of an agitated tubular reactor (ATR) for intensification of chemical processes

Hugh P. Rice [a,b,1,*], Yi He [a,1], Frans L. Muller [a,c], Andrew E. Bayly [a], Robert Ashe [d], Andrew Karras [d], Ali Hassanpour [a], Richard A. Bourne [a,c], Michael Fairweather [a], Timothy N. Hunter [a]

[a] School of Chemical and Process Engineering, University of Leeds, Leeds LS2 9JT, UK
[b] School of Mechanical Engineering, University of Leeds, Leeds LS2 9JT, UK
[c] School of Chemistry, University of Leeds, Leeds LS2 9JT, UK
[d] AM Technology, Unit 18 Berkeley Court, Runcorn, Cheshire WA7 1TQ, UK

ARTICLE INFO

Keywords:
Agitated reactor
Lattice Boltzmann methods (LBM)
Intensified plug-flow
Mixing dynamics
Process intensification

ABSTRACT

This study investigates the dynamics of a novel, oscillatory, intensified plug-flow reactor – an agitated tubular reactor (ATR) – designed for efficient flow processing of solid-liquid mixtures. The relative movement of the reactor and agitator bar, and associated effects on fluid mixing, were characterised physically with a suite of experimental instruments – utilising laser-based, video-based and acoustic techniques – and numerically *via* a Lattice Boltzmann method (LBM) computational fluid dynamic simulation. The reactor volume consisted of a cylindrical outer tube containing a free-moving, perforated agitator tube. The position, velocity and angular velocity of the inner agitator relative to the outer tube were measured experimentally and computationally under a range of realistic operating conditions, in terms of applied agitation frequency and displacement distance, along with their effect on the associated fluid velocity and turbulence levels. Additionally, simulations were used to validate a model for the reactor power input. The agreement between experimental and simulation data was very good in all cases, leading to clear recommendations for optimal operating conditions, while an experimentally derived regime map of the types and magnitudes of ATR motion is also presented.

1. Introduction

Flow reactors are increasingly popular in the chemical industries, as they offer numerous advantages over batch reactors [1-7]. Scale reduction in a key aspect of chemical process intensification, the benefits of which are (a) enhanced performance of smaller equipment, and (b) more efficient use of existing laboratory space and instruments, or a combination thereof [8]. Flow reactors lead to inherently faster reaction kinetics and higher yields (due to improved mixing, mass and heat transfer) and can be run and optimised continuously, with potential associated space savings [1]. By comparison, the productive operating time of large batch reactors is generally very low, and a typical batch plant will use a number of reactors of various sizes to cope with variations in working volume requirements. This inherent difference in efficiency means that a small number of continuous flow reactors could replace many large batch reactors, and so deliver substantial reductions in capital expenditure and operating costs [9].

The advantages of flow reactors have driven their adoption in industrial process intensification. However, traditional passively mixed plug-flow reactors have an important limitation, namely short residence times for reactions requiring highly turbulent flows to ensure good mixing [10,11]. This limitation is particularly significant for long-residence-time reactions or multiphase systems involving solids – or any high-density-contrast mixtures – as plug-flow reactors generally do not have the capacity to pump at flow rates sufficiently high to keep the solid phase suspended. The result is that flow reactors suffer from increased particle-phase sedimentation, fouling at inlets/outlets and an associated reduction in the mixing efficiency and reaction rate [8].

Flow chemistry is a crucial part of process intensification, and its widespread adoption is contingent on the development of reactors that

* Corresponding author at: School of Chemical and Process Engineering, University of Leeds, Leeds LS2 9JT, UK.
E-mail address: h.p.rice@leeds.ac.uk (H.P. Rice).
[1] These authors contributed equally to this work.

https://doi.org/10.1016/j.cep.2022.109067
Received 20 May 2022; Received in revised form 14 July 2022; Accepted 21 July 2022
Available online 22 July 2022

can handle significant solids loading, where the ability of passively mixed reactors to process multiphase systems is generally only possible with small, slow-settling particles and over short reaction times. Therefore, a number of intensified flow reactor technologies has been investigated over recent years for this purpose. Of those that are more easily scalable, rotational reactors, such as spinning disc reactors or rotating packed bed reactors, have been widely researched [8,12-15], where centripetal forces act to dramatically enhance mass transfer and reaction kinetics. The limitation of using accelerated rotational motion is that residence times through the reactor are therefore small and dependent on the rotation rate. Inline static mixers have also been used to generate enhanced mixing and turbulence with relatively low bulk flow rates, although maintenance of a homogeneous dispersion is still dependent on flow rate, and fouling is a significant issue for solids processing [16,17].

Technologies that decouple mixing from the axial velocity are therefore highly advantageous. Perhaps the most well-known are oscillatory baffle reactors (OBRs) [12,18,19], where the insertion of, normally, disc or orifice baffles combined with pulsed oscillations (of the order of a few Hz) that are separated from the main driving flow, can greatly enhance shear mixing. Modern systems also combine OBRs with intensified reaction systems, such as inline microwave applicators [20]. However, as with inline mixers, the baffles can instigate fouling in multiphase reacting or catalytic systems, while more generally, solid-liquid dispersion and back-mixing is a complex issue that is significantly affected by oscillation rate and baffle area, for example [19]. While non-baffled oscillatory flow reactors also exist, utilising split flows [21,22] or coils to initiate Dean vortices [18,23], scale-up can be challenging in such designs.

As an alternative, agitated reactors are intended to overcome many of the problems described above. They also operate by oscillatory mechanical driving of the working part of the reactor in order that flow and mixing are mechanically decoupled and can therefore be controlled independently [24-28]. However, with these reactor designs, the problems related to mixing in plug-flow is resolved by using a secondary, loose agitator baffle inserted into the main reactor. A fast, lateral (*i.e.* radial) oscillation is applied to the main body of the reactor (as opposed to the streamwise direction of oscillation in an OBR) where the relative motion of the secondary tube is intended to enhance mixing and inhibit gravitational phase separation, in a configuration that is considerably less susceptible to fouling.

To date, laboratory scale agitated cell reactors (ACRs) have been the more widely researched of these reactor designs. They work on the principle of a cascade of randomly mixed stages, and have been used for a variety of purposes including solids-catalysed organic synthesis and organic crystal production [27,29-32], as well as the eco-friendly production of inorganic nanoparticles [33]. Larger agitated tubular reactors (ATRs) that have single radial mixing stages are an emerging area of interest, owing to their scale-up potential. In foundation work, Jones et al. [34] compared ACRs and ATRs for scaled continuous biocatalytic reactions, while Filipponi et al. [26] investigated their use for the production of triacetic acid lactone at a kilogram scale. More recently, ATRs have been used as flow reactors to produce composite metal hydroxide precipitates for dye removal [28], intensified ion exchange systems [35] and liquid-liquid contactors [36], while there have been some initial investigations into the mixing and dispersion characteristics of ATRs using computational fluid dynamic (CFD) simulations [37,38].

Despite this research interest in ATRs, there is a lack of comprehensive understanding of how the dynamics of the agitator bar aids dispersion of multiphase suspensions, and the limitations of this approach to mixing. Therefore, to overcome this significant knowledge gap, this study comprises a description, demonstration and physical and numerical characterisation of an agitated tubular reactor – specifically, the Coflore® ATR, designed by AM Technology – which is presented as a novel, intensified plug-flow reactor suitable for a variety of solid-liquid chemical processing operations. Through characterisation of the system, the critical objective is to better understand the mechanical motion and hydrodynamics within the ATR [37], in order to allow for optimisation of the reactor with catalysed solid-liquid chemical reactions. Experimentally, a suite of techniques is used, including laser displacement, image analysis and ultrasonic Doppler profiling, to fully measure and describe the relative motions of the outer tube and inner agitator, as well as the associated liquid velocities through the reactor. This experimental data is also used to validate an innovative lattice Boltzmann method (LBM) numerical CFD simulation of the same system, allowing for further examination of the coupling of the fluid to the agitator. Additionally, numerical simulations are used to develop a model for the working power per unit volume of the reactor.

2. Materials and methods

2.1. Coflore® agitated tubular reactor and materials

A pilot-scale Coflore® agitated tubular reactor was used (AM Technology, U.K.) as shown in Fig. 1. It has a nominal maximum reactor volume of 1 litre and can be operated with up to ten reactor tubes of 100–150 ml each, of which any number can be used in series or parallel. Into each is inserted a perforated agitator tube that is free to move upon mechanical driving of the ATR body (see inset, Fig. 1(a)). The system is driven by pneumatic actuators, and its bulk lateral motion can be characterised by an agitation frequency, f, specified by the user *via* the control box shown on the left of Fig. 1(a), and an amplitude, a, determined by the pressure applied *via* an air valve below the main body of the ATR. For the experimental investigations reported here, a separate, transparent Perspex test reactor tube was built and installed on top of the main reactor, with the exact same dimensions as the regular tubes, to facilitate movement characterisation *via* visual and ultrasonic methods (see following section). The reactor tube had an inner diameter of 25.4 mm (3 mm wall thickness) and 392 mm total length, with an inner perforated stainless steel agitator tube of 13.8 mm inner diameter (0.6 mm wall thickness) [35]. The working volume of the reactor tube was approximately 150 ml [28].

Most experiments performed for this study used a single working fluid of pure water within the reactor, although some additional experiments were conducted with dispersions of palladium-loaded activated carbon catalyst particles (Johnson Matthey, UK) to investigate the ATR's ability to disperse candidate solid phases. The particles had a mean diameter of around 20 μm and a density of 2500 kg/m^3.

In addition, because the main objective of the study was to understand the mixing action of the agitator, there was no bulk liquid flow through the reactor, so the effect of bulk fluid velocities and shear were ignored for simplicity. Nevertheless, given the nominal reactor operating conditions (of the order of 5 ml/min for a 30 min residence time) the relative effects of this motion on fluid shear are expected to be negligible.

2.2. Experimental methods

Optical and laser-based techniques have long been used for investigation of flow in complex reactor vessels [39]. For example, laser Doppler anemometry [40,41], particle image velocimetry [42] and planar laser-induced fluorescence [43] have been used successfully to interrogate the flow dynamics and reaction behaviour within such vessels. However, these techniques require fine positional calibration that would be difficult with oscillating measurement domains such as those present in ATRs.

Therefore, a suite of instruments was designed that would avoid the difficulties associated with measuring a rapidly moving reactor vessel. The techniques chosen to characterise the motion of the ATR, and the fluid motion within it, consisted of an external laser displacement device (to measure the bulk motion of the outer tube), high-speed video cameras (motion and rotation of inner and outer tubes) and an ultrasonic

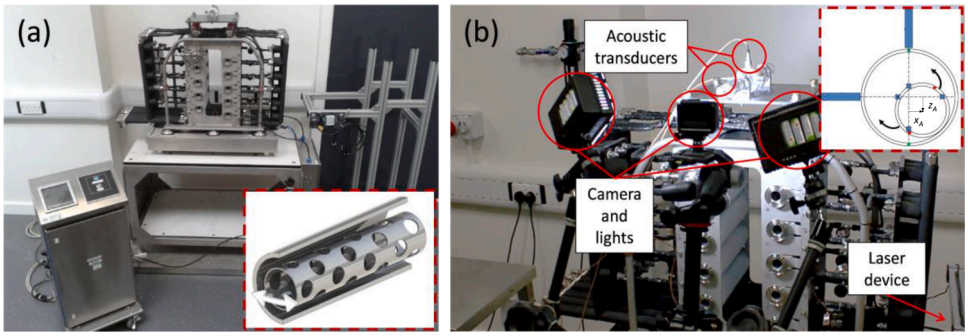

Fig. 1. (a) Photographic image of Coflore® ATR (inset: 3D render of agitator-tube arrangement); (b) close-up image of ancillary equipment, including transparent test reactor tube with camera, laser and acoustic transducers (inset: schematic of transducer arrangement on reactor tube). Relative position of inner to outer tube indicated by "x_A" (horizontal) and "z_A" (vertical) in schematic.

profiler (motion of inner tube and fluid velocity and turbulence intensity fields). To the authors' knowledge, this is the first time such an experimental suite has been used to non-intrusively measure the complex flow structure of this type of process-intensified reactor. The suite of experimental measurement apparatus is shown in Fig. 1(b) and is described in more detail below.

2.3. High-speed video and image analysis

Two high-speed video cameras (Canon EOS 550D for initial testing of the system and validation of data processing, 60 frames per second; GoPro HERO5 for the main body of experiments, 240 frames per second) both with an image resolution of 720p (*i.e.* 1280 by 720 pixels) were used to record images of the ATR motion. Coloured plastic studs of different colours (outer tube: green; inner tube: orange-red) were attached to the ends of the test tube to allow tracking *via* video image analysis. The cameras were positioned to record the tube and agitator movement end-on, and the area was illuminated by two banks of LED lights (see Fig. 1(b)). The images were then post-processed with custom-written MATLAB® code (The MathWorks, Inc.) to extract the position of the outer tube relative to the stationary camera and that of the inner agitator bar relative to the outer tube. The process of extracting the positions of the inner and outer tubes of the ATR is described in more detail below, and consists of (a) identifying the positions of coloured markers attached to the ends of each tube (two markers per tube), (b) calculating the absolute position of the outer tube over time, then (c) calculating the absolute and relative position of the inner, loose agitator tube. The velocity of both tubes, and the angle and angular velocity of the inner tube, which can rotate, could then be calculated from the positional time-series data.

By inspection of individual video frames during which the ATR was stationary (see example in Fig. 2(a)), representative RGB (red-green-blue) values of the two reference tracking colours (orange-red and green) were determined. In general, these reference values varied between runs according to ambient light levels. The colour difference between every pixel and each of the two reference colours was calculated, *i.e.* the Euclidean distance in a simple RGB colour-space [44], as in Fig. 2(b). All pixels within a certain colour-distance threshold – determined by trial and error such that the correct regions were highlighted and the width of the tracking points were accurately reproduced – were identified and a binary map generated (see Fig. 2(c)). As with the RGB reference values for the tracking colours, the thresholds varied to some extent between runs according to ambient light conditions.

Once the central points (centroids) of the outer (green) tracking points were identified, the distance-to-pixel ratio – *i.e.* the effective spatial resolution of the image analysis method – could be determined (from images in which the ATR was stationary) using the known separation between them, which was measured manually for reference and calibration. In general, the distance-to-pixel ratio was around 0.15 mm per pixel. The centroids of the tracking markers were identified and their position, velocity and angular velocity tracked over a period of 10 s for each run. A median-value averaging filter was applied to the positional data, the parameters of which were varied between runs and according to lighting conditions. The same procedure was applied to the inner agitator bar (orange-red markers) by altering the parameters of the colour filter. The relative motion of the inner tube was derived by subtracting its position – specifically, the central point of its two markers – from the central position of the outer tube.

2.4. Acoustic backscatter profiling and Doppler velocimetry

An acoustic measurement system, the UVP-DUO™ (Met-Flow, Lausanne, Switzerland) is hereafter referred to as the UVP based on its primary function as an ultrasonic velocity profiler. The system was used both as a velocity profiler, to measure the velocity field along a profile through the outer tube, and as an acoustic backscatter device, to measure the position of the inner agitator tube relative to the outer tube, for validation purposes, as described in detail below. The basic mode of operation of the UVP is as follows: a known voltage for a known number of cycles is applied to a piezoelectric emitter-receiver transducer (hereafter referred to as a probe), which is thereby caused to oscillate at that frequency and transmit an acoustic pulse into the measurement domain [45]. Objects – in this study, solid boundaries (for measuring the position of the inner agitator tube; see below) and suspended particles

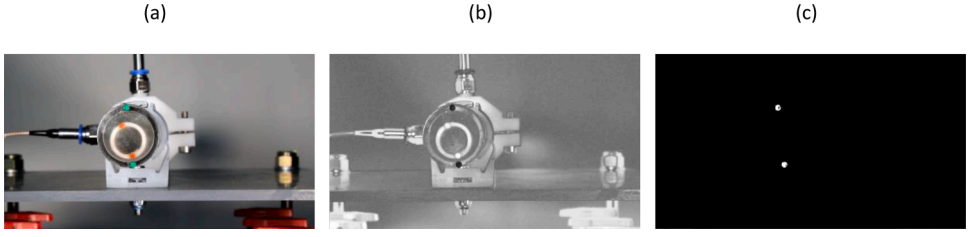

Fig. 2. Example of high-speed video image capture and analysis method. (a) Raw RGB colour image; (b) green colour filter applied, with green areas shown as darker; (c) binary version of image with threshold applied for identification of outer tube tracking points.

(for measuring the fluid velocity field) – reflect some of the incident acoustic energy back towards the transducer, causing it to vibrate and thereby exciting a voltage in it. The voltage time-series data are then used to determine the position and dynamics of objects in the measurement domain [46].

The general acoustic backscatter method is described elsewhere [47-50] and consists of identifying a peak in the backscatter profile, the position of which corresponds to the side of the agitator tube closest to the acoustic transducer, and the fundamental property of the agitator tube being exploited is its acoustic reflectivity. Two 4 MHz transducers were mounted onto the outer side of the test tube with a bespoke probe holder, where a section of the outer tube wall was filed flat to ensure a flush transducer connection and strong acoustic penetration. Probes were connected in both horizontal and vertical directions (see inset, Fig. 1(b)), although in the work presented here, only the horizontal probe data are analysed. The acoustic backscatter method was used for cross-validation of the other measurement methods (see Section 2.2.4). However, it was not used later in the study as its spatial resolution (0.37 mm at a fundamental frequency of 4 MHz) is below that of the video system (approximately 0.15 mm per pixel).

The same UVP system was also used as a Doppler velocimeter [51-53] to record the fluid velocity field in the same measurement domain (*i.e.* horizontally through the outer tube) and using the same measurement parameters described above (*i.e.* 0.37 mm spatial resolution, 4 MHz fundamental frequency). Acoustic velocimetry relies on the Doppler effect such that the fundamental frequency of the acoustic pulses (here 4 MHz) reflected by objects in the measurement domain is shifted by some amount, Δf, corresponding to the objects' velocity relative to the measurement device, according to the Doppler equation [54]. In practice, the UVP calculates this frequency shift using a fast Fourier transform of the time-series voltage data [55]. In this way, the velocity of acoustic scatterers (here, suspended solid particles, whose motion is used as a proxy for fluid motion) is profiled through the measurement domain.

Acoustic beam divergence is a known limitation of acoustic measurement systems of this type [39,45]. However, the divergence angle for the transducer used here is around 2° [56], which is expected to have a negligible effect on the measurements presented. The measurement domain of the acoustic system is a conical frustum orientated laterally (*i.e.* radially) through the reactor tube, and measurements are effectively averaged over a cross-sectional area with a radius of 2.80 mm at the near side of the domain and 3.76 mm at the far side.

2.5. Laser displacement device

An ILD1320-50 laser-optical displacement sensor (Micro-Epsilon, Birkenhead, UK) including proprietary software provided by the manufacturer, was used for measuring the bulk motion of the ATR and therefore the outer tube. The sample rate was 1 kHz, the operating range 35–85 mm from the device, and the spatial resolution 5 μm. The device's stand (KJN, Leicester, UK) and mounting were designed and assembled at the University of Leeds. The laser was directed perpendicularly at a flat, vertical steel face of the stationary part of ATR (on the lower right of the device, as it is shown in Fig. 1(a)).

2.6. Validation of experimental methods

For the purpose of validation between the suite of experimental methods used, an initial comparison of the various experimental measurement methods was made, as shown in Fig. 3 for two runs, both at $f \approx$ 4 Hz, but with different values of the amplitude, a. In Fig. 3(a), in which $a \approx 2.8$ mm, data from the acoustic backscatter and video image analysis are compared, with the agreement being excellent; the spatial resolution of both systems is also evident (acoustic: 0.37 mm; video: 0.15 mm approx.). In Fig. 3(b), data from the high-speed video analysis and the laser device are compared for the outer tube ($a \approx 8$ mm) and the agreement is also excellent, giving confidence in the methods used throughout this study. It is noted that the data in Fig. 3(b) have been centred for visualisation purposes such that they fit Eq. (3), with $b = 0$. In general, and as shown in the inset schematic in Fig. 1(a), the position of the inner tube is defined relative to the outer tube, such that its position is $(x_A, z_A) = (0,0)$ when the tubes' centres are coincident.

2.7. Numerical model and CFD simulation

In the ATR system, agitation is driven by the lateral oscillation of the external tube. Consequently, the motion of the internal agitator is controlled by both fluid motion and the contact force between the agitator and the tube. Modelling of the ATR system thus requires that fluid-structure and structure-structure interactions be accounted for simultaneously. In the present study, a recently developed CFD model, coupling a soft-sphere collision model with dynamic meshing [37], is extended to a lattice Boltzmann method (LBM) framework, due to its superior computational efficiency. The LBM code is based on that reported by Derksen and Van den Akker [57] and was adapted for GPU execution. It is a second-order discretisation of the incompressible Navier-Stokes equations in both space and time solved on a cubic lattice. The turbulent flow is modelled using a large eddy simulation approach, with a conventional Smagorinsky subgrid-scale (SGS) model [57]. An immersed boundary approach is applied to enforce the no-slip boundary condition on the solid surfaces of the shaking tube and the agitator. The code was validated in the same way as reported in a previous study [37] by comparison with the falling sphere experiments of Ten Cate et al. [58].

Fig. 4(a) presents a schematic of the modelling geometry, in which the internal agitator is treated as a single discrete element.

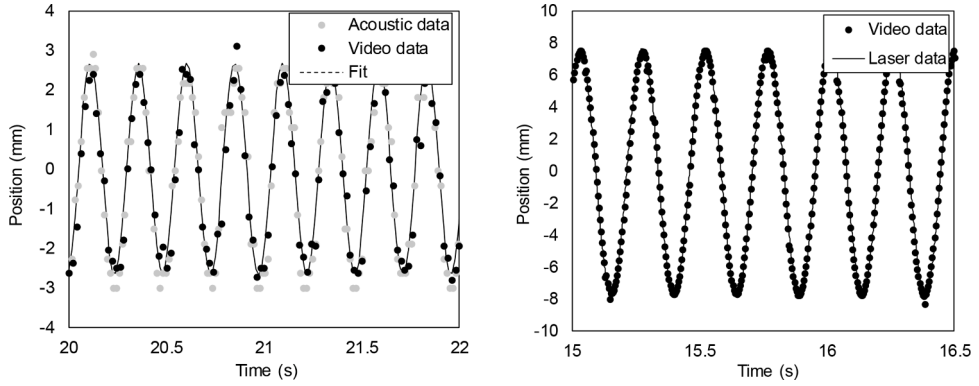

Fig. 3. Left: horizontal position of inner agitator relative to outer tube, as measured with acoustic backscatter and video data (where dashed line is a sinusoidal fit). Right: position of outer tube, as measured with high-speed video and laser device data. Both data sets at $f \approx 4$ Hz (different amplitudes).

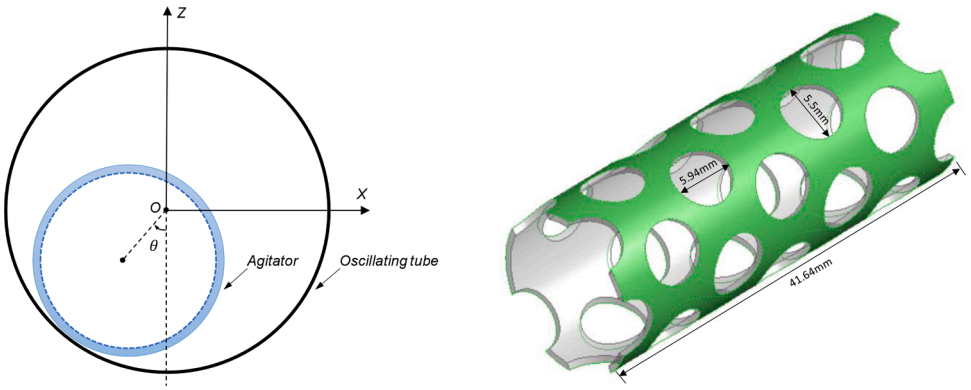

Fig. 4. Left: schematic of modelling configuration. Right: modelled geometry of ATR system.

For an internal agitator of mass m and radius R, the governing equation of the motion can be written as:

$$m\frac{d\mathbf{v}}{dt} = \mathbf{F}_f + \mathbf{F}_c + m\mathbf{g}, \tag{1}$$

$$I\frac{d\omega}{dt} = \mathbf{T}_f + \mathbf{T}_c, \tag{2}$$

where F_f and T_f are the force and torques due to the hydrodynamic effect, and F_c is the force due to collision with the external oscillating tube, including both normal and tangential contact forces and damping forces. The torque T_c consists of contributions from the tangential contact force and rolling resistance. The collision between the agitator and the external tube is modelled by the same soft-sphere collision model used in a previous study by the current authors [37]. Table 1 summaries the equations used for the calculation of these forces, where the effective elastic modulus is calculated as $E = Y/(1-\nu^2)$, with Y being the Young's modulus and ν the Poisson ratio for the internal agitator. Here, $\delta_{t,\max}$ is the critical tangential displacement such that $\delta_{t,\max} = \mu_t\delta_n(2-\nu)/(2-2\nu)$, which distinguishes the friction state as static friction or dynamic sliding friction.

The internal agitator is a perforated tube, as shown in Fig. 4(b). Only a 41.6 mm section of the ATR system is modelled, with periodic boundary conditions applied in the axial direction to reduce computational cost. Water is used as the working fluid. No pressure gradient is applied (*i.e.* there is no bulk axial longitudinal flow) which is consistent with the experimental setup. The specific values for the full list of parameters used in the numerical simulations are shown in Table 2.

2.8. Operating conditions of CFD simulation test cases

The lateral motion of the ATR was modelled as sinusoidal. The displacement, A, and lateral velocity, U, of the external tube are as follows in Eqs. (3) and (4):

Table 1
Equations used to calculate forces and torques in this work [37].

Terms	Equation
Fluid force	$\mathbf{F}_f = \oiint \boldsymbol{\sigma}\cdot\hat{\mathbf{n}}dS$
Fluid torque	$\mathbf{T}_f = \oiint \mathbf{R}\times(\boldsymbol{\sigma}\cdot\hat{\mathbf{n}})dS$
Normal contact force	$\mathbf{F}_n = \frac{4}{3}ER^{1/2}\delta_n^{3/2}\hat{\mathbf{n}}$
Normal damping force	$\mathbf{F}_{d,n} = -c_n(8mE\sqrt{R\delta_n})^{1/2}\mathbf{v}_n$
Tangential contact force	$\mathbf{F}_t = -\frac{\boldsymbol{\delta}_t\mu_t\lvert\mathbf{F}_n\rvert}{\lvert\boldsymbol{\delta}_t\rvert}\left[1-\left(1-\frac{\min(\lvert\boldsymbol{\delta}_t\rvert,\delta_{t,\max})}{\delta_{t,\max}}\right)^{3/2}\right]$
Tangential damping force	$\mathbf{F}_{d,t} = -c_t\left(6\mu_t mE\lvert\mathbf{F}_n\rvert\frac{\sqrt{1-\lvert\boldsymbol{\delta}_t\rvert/\delta_{t,\max}}}{\delta_{t,\max}}\right)^{1/2}\times\mathbf{v}_t$
Rolling torque	$\mathbf{T}_c = (\mathbf{F}_t+\mathbf{F}_{d,t})\times\mathbf{R}+\mu_r R\lvert\mathbf{F}_n\rvert\hat{\boldsymbol{\omega}}_n$

Table 2
Parameters used in the simulations.

Parameter	Value
Tube diameter (mm)	25.4
Outer diameter of agitator (mm)	15.0
Inner diameter of agitator (mm)	13.8
Length of agitator segment (mm)	41.6
Cap thickness (mm)	1.5
Density of agitator (kg/m^3)	7800
Moment of inertia of agitator (kg•m^2)	2.516×10^{-7}
Young's modulus of agitator, Y(Pa)	1.0×10^{8}
Poisson ratio of agitator, ν	0.3
Sliding friction coefficient of agitator, μ_r	0.1
Rolling friction coefficient of agitator, μ_t	0.05
Damping coefficient of agitator	0.3
Fluid density, ρ (kg m^{-3})	998.2
Fluid viscosity, μ (kg m^{-1} s^{-1} or Pa s)	0.001
Grid size (mm)	0.2
Time step (s)	10^{-4}

$$A(t) = a\sin(\omega t+\alpha)+b, \tag{3}$$

$$U(t) = a\omega\cos(\omega t+\alpha), \tag{4}$$

where a is the amplitude, ω is the angular frequency such that $\omega = 2\pi f$, α is an angular offset and b is a linear offset to account for the mechanical position of the ATR relative to the measuring instrument. In practice, the maximum displacement of the ATR is limited to $a = 12.5$ mm by mechanical buffers (notwithstanding flexibility in the fabric of the ATR and its fixings, which can result in $a > 12.5$ mm in practice) and the practical range of agitation frequencies is $1 \lesssim f\,(\mathrm{Hz}) \lesssim 6$. The motion of the inner agitator bar can also be modelled as a sinusoidal, but the values of the amplitude, a, will be very different to the amplitude of the outer tube (see Fig. 3 for an example of the agitator *versus* outer tube amplitude and Section 3.2 for a more detailed discussion of the relative amplitudes involved). As described earlier, the horizontal and vertical positions of the inner tube, x_A and z_A, are defined as (0,0) when the tubes' centres are coincident.

Three test cases were chosen for direct comparison of experimental observations of agitator motion to numerical results. The conditions in the test cases generally represent optimal operating conditions in terms

Table 3
Operating conditions of three test cases chosen for experimental-numerical comparison.

Case	Frequency, f (Hz)	Amplitude, a (mm)
1 (base)	5.00	12.5
2	4.07	10.2
3	3.13	11.2

of agitation frequency and applied pneumatic pressure and are given in Table 3. Case 1 was used as a reference case, based upon manufacturer recommendations for optimal oscillation frequency (5 Hz) and the maximum nominal device displacement. It was used to calibrate the key parameters in the numerical model (*i.e.* the sliding and rolling friction coefficients). Once calibrated, fixed values of these parameters were used for all cases. Cases 2 and 3 represent optimal experimentally determined motion for nominal agitation frequencies of 3 and 4 Hz, with the exact frequencies found from the experimental data (see Results and Discussion, Section 3.1). They therefore represent two further direct comparisons to experimental results for validation purposes.

3. Results and discussion

3.1. Experimental regime mapping of ATR motion

The two experimental control parameters – agitation frequency and applied pneumatic pressure – were varied in order to construct a regime map of ATR motion, in terms of the type of motion and amplitude, as defined in Eq. (3). The displacement was measured with the laser device, and the regime map is presented in Fig. 5.

There is a range of applied pressures (or displacement amplitudes) where motion is nominally sinusoidal. At low pressure, inertia from the ATR mass inhibits motion, while at high pressures, there was evidence of mechanical knocking, as the ATR contacted the internal buffers at its extremities of motion, which caused some secondary non-sinusoidal motion. For the highest frequency (6 Hz) it was also apparent there was mechanical inertial lag, where the ATR movement is reversed before fully being able to accelerate to its maximum lateral displacement in either direction. Hence, the actual displacement amplitudes for the 6 Hz cases were markedly smaller (see Fig. 5(b)). In general, the regime map suggests optimal sinusoidal motion occurs within a frequency range of 3–5 Hz, with amplitudes below the maximum available displacement (of 12. 5 mm). It should also be noted that the values of the displacement, a, given in Fig. 5(b) in some cases exceed this nominal maximum amplitude of 12.5 mm, dictated by the internal mechanical buffers, because the body of the ATR is able to flex slightly, to the order of a few millimetres. (Blank cells in Fig. 5 are shown as such to illustrate range of realistic operating states; outside that range, a risk of mechanical damage was present.)

Three examples of the ATR motion – those marked with asterisks in

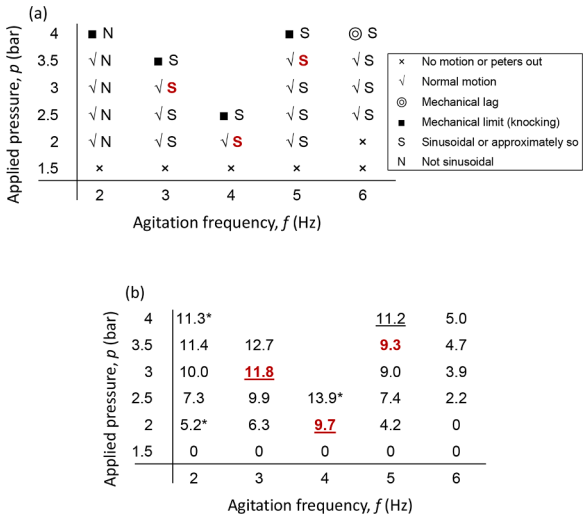

Fig. 5. Regime map of ATR motion, showing influence of applied pressure and oscillation frequency on (a) nominal sinusoidal motion and (b) oscillation amplitude. Red-bold: optimal conditions at 3–5 Hz; underlined: test cases compared to numerical simulations. Cases marked with asterisk (*) further analysed in Fig. 6.

Fig. 5 – are given in Fig. 6, where the absolute position (measured with the laser device) is presented for a number of agitation frequencies and applied pressures. As is clear from Fig. 6(a) and (b), the ATR motion is non-sinusoidal at lower agitation frequencies due to the action of internal mechanical buffers. Fig. 6(c) shows that the motion is sinusoidal with no knocking at a device "sweet spot", such as at $f = 4$ Hz, $p = 2.5$ bar, *i.e.* the conditions at which maximum displacement and smooth, sinusoidal motion is achieved with minimal applied pneumatic pressure. Here, it is noted that in all cases, the actual measured oscillation frequency, from the fitted sinusoidal curve, was slightly different to the nominal mean values (*e.g.* 4.05 Hz for the nominal case of 4 Hz). Hence, as discussed for the simulation test cases, the actual, experimentally measured agitation frequencies were used for the validation runs. It is important to note that the amplitudes for the three test cases given in Table 3 do not correspond exactly to the sweet spots in Fig. 5, as it was difficult to recreate the same operating conditions in multiple runs, because the valve used to control the applied pressure was very sensitive.

3.2. Agitator and fluid motion

Results for the agitator position and motion are shown in Fig. 7, in time-series form for an example one-second interval, where the experimental results from the high-speed video analysis are compared directly to the numerical simulations for the three test cases, as given in Table 3 ((i) to (iii), top to bottom of Fig. 7). Here, the position of the centre of the agitator is plotted in coordinates relative to the centre of the outer reactor tube, as shown schematically in Fig. 4, in terms of the horizontal position, x_A (given in Fig. 7(a)), and vertical position, z_A (Fig. 7(b)).

Overall, the agreement between experiment and simulation is very good in terms of the periodicity and magnitude of motion. As with the movement of the outer tube, both simulations and experiments predict a largely sinusoidal movement of the inner agitator bar (which is generally out of phase with the outer tube). The vertical motion, which also follows an approximately sinusoidal path, is caused by the agitator rolling upwards on the outer tube at the extremities of displacement. The actual relative displacement of the inner agitator is, of course, much smaller than the displacement amplitude of the outer tube as it is contained within it, with horizontal amplitudes of about 3 mm for the 4 and 5 Hz cases, and 2 mm for the 2 Hz, with vertical amplitudes of 1–2 mm.

The simulations predict a horizontal position (Fig. 7(a), frames (i) to (iii)) that is slightly above the experimental results, especially for Case 1 (i) and Case 3 (iii), while a better match can be seen in the vertical direction (frames (b)). It is also noted that there the agreement is closest between numerical and experimental results for Cases 2, which represents the most sinusoidal-like motion. The discrepancies are likely to do with the mechanical properties of the experimental system. For example, as discussed, the overall amplitude of the ATR at 5 Hz (Case 1) was slightly below that of the maximum amplitude used in the simulation, due to system inertia. Additionally, the experimental system at 5 Hz was run at its mechanical limit, where some knocking occurred, as can be seen in the slight deviation from sinusoidal motion at the extremities of displacement. This mechanical knocking and flexibility in the physical system is even clearer in the 3 Hz experimental data (Case 3, (iii)) where the motion diverges from ideal sinusoidal motion in the experimentally measured horizontal positional data.

The path of motion of the agitator is given for the three test cases, by comparing the vertical to horizontal displacement, in the third column of Fig. 7, *i.e.* (c), frames (i) to (iii). The measured amplitude of the agitator motion, and the extent to which it rolls up the inner wall of the reactor tube, are well matched by the numerical model. Additionally, though, experimental data suggest that the agitator leaves the surface of the outer tube at the extremes of its motion. This behaviour is clearest in Case 1 (in which the agitation frequency and amplitude are greatest) where the agitator traces out a figure-of-eight-like motion, although there is some scatter in the data at the positional extremes. The

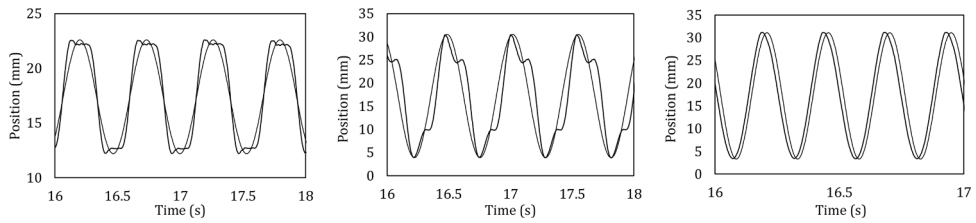

Fig. 6. Lateral motion of ATR (solid line) measured with laser device at (a) $f = 2$ Hz (nominal), $f_a = 1.88$ Hz (actual), $p = 2$ bar, $a = 5.2$ mm, (b) $f = 2$ Hz, $f_a = 1.88$ Hz, $p = 4$ bar, $a = 13.3$ mm, and (c) $f = 4$ Hz, $f_a = 4.05$ Hz, $p = 2.5$ bar, $a = 13.9$ mm, with fitted sinusoid (dashed lines). Offset in (c) added for illustration.

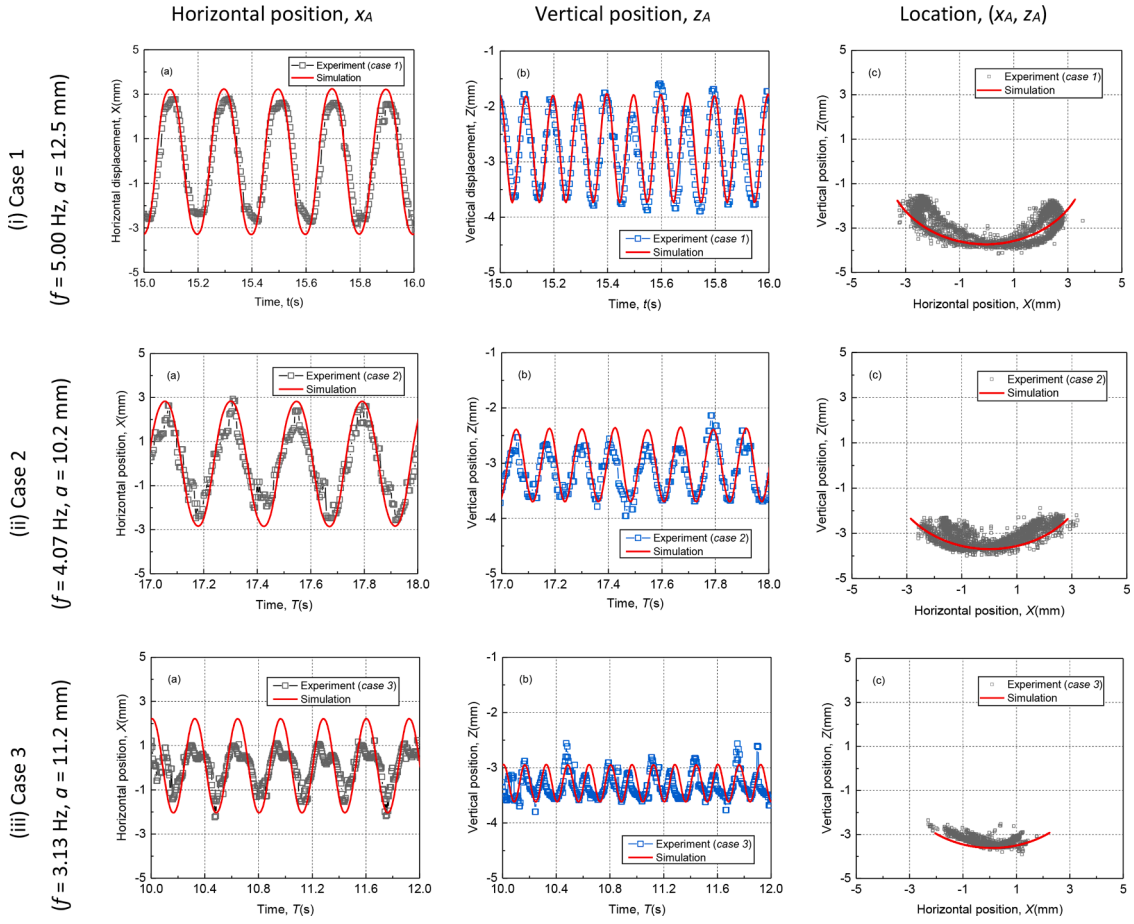

Fig. 7. Direct comparison between experimental high-speed video analysis and CFD simulation of agitator movement. Shown is agitator centre relative to centre of reactor tube, in terms of (a) its horizontal position, x_A, (b) vertical position, z_A, and (c) horizontal *versus* vertical position. Data given for three test cases at nominal oscillation frequencies of 5 Hz (i), 4 Hz (ii) and 3 Hz (iii), top to bottom of figure.

numerical simulation predicts that the agitator tube rolls and slides along the internal wall of the outer tube without leaving the surface, irrespective of the operating conditions. The extent of separation between the agitator and the reactor wall in the experimental results is, however, very small (around 1 mm). It is likely to be influenced by mechanical flexibility of the moving platform onto which the ATR device is mounted or potentially elasticity in the PTFE boots that protect the ends of the agitator bar.

Results from the high-speed video data and simulations for the velocity distribution of the agitator bar are shown in Fig. 8 for the three test cases (as before, (i) to (iii), top to bottom of figure). Here, the experimental velocity data were extracted from the change in positional data for the horizontal component, $U_{A,x}$ (a), and vertical component, $U_{A,z}$ (b). A comparison of the angular velocity, ω_A, centred around the inner agitator, is also given (Fig. 8(c)).

The agreement between experimental and numerical results is again very good for the agitator tube velocity data (Fig. 8). There is some scatter in the experimental velocity data, especially at the extremities of motion, as the velocity and angular velocity data are themselves derived from multiple positional data, so small finite errors accumulate. This is particularly true of the lowest oscillation frequency (Case 3), and it is noted that in this case the amplitude of motion is smaller and is, in fact, close to the measurement limit of the apparatus, i.e. the spatial resolution of the video data from which the plots are derived. Practically, the velocity data confirm that the agitation motion strongly influences the peak shear imparted on the fluid by the agitator, with a velocity change of around ±100 mm/s for the 5 Hz case and ±75 mm/s for the 4 Hz case, which reduces markedly to around ±40 mm/s for the 3 Hz case.

These velocity values can be used to estimate the level of turbulent mixing using a modified radial mixing Reynolds number, Re_r, defined in Eq. (5), where D_A is the agitator diameter and U_{max} can be defined as the maximum horizontal velocity from the given oscillation rate and

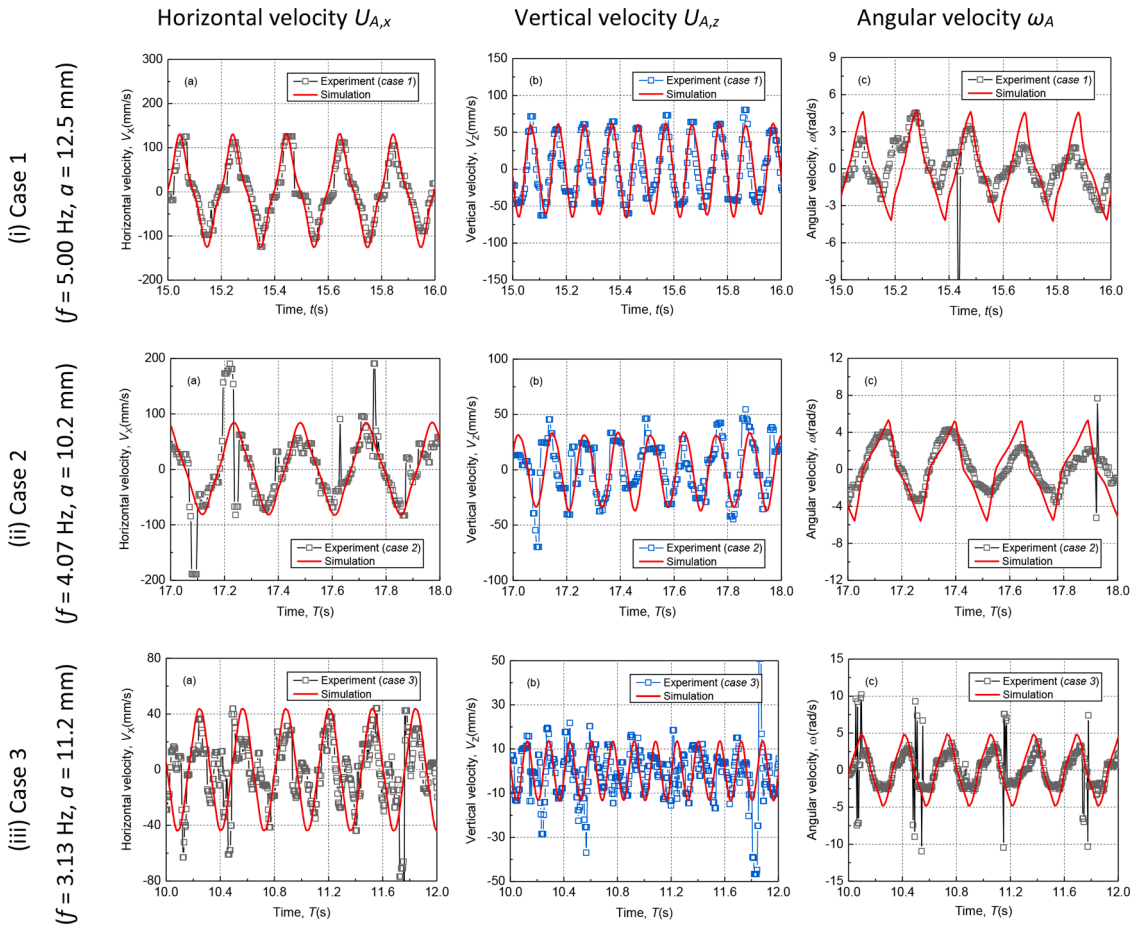

Fig. 8. Direct comparison between experimental high-speed video analysis and CFD simulation of agitator velocities relative to centre of reactor tube, in terms of (a) horizontal velocity, (b) vertical velocity and (c) angular velocity. Data given for three test cases at nominal oscillation frequencies of 5 Hz (i), 4 Hz (ii) and 3 Hz (iii), top to bottom of figure.

horizontal amplitude ($U_{\max} = 2\pi fa$):

$$Re_r = \rho_L D_A U_{\max}/\mu_L. \quad (5)$$

Previously in simulations of the ATR, this Reynolds number has been calculated based on the amplitude of the outer tube [37,38]. However, given that it is the relative motion of the agitator that is critical, the amplitude of the agitator motion is more appropriate, which can be taken from Fig. 7(a) for the three test cases from experimental data (taking only the horizontal component). This gives $Re_r \approx 1300$, 1033 and 520 for the 5 Hz, 4 Hz and 3 Hz cases, respectively, where an amplitude $a = 3$ mm is used for the 5 and 4 Hz cases, and 2 mm for the 3 Hz case. These estimates are based on perfect translation of the oscillatory motion of the agitator. For comparison, the maximum horizontal velocities measured or simulated (Fig. 8) can also be used as an estimate for $U_{\max}$ (assuming that the maximum measured horizontal velocity occurs with the agitator in the centre of its motion, and hence is equivalent to the translated radial velocity). Using these $U_{\max}$ values (as described in Fig. 8) yields $Re_r \approx 1500$, 1028 and 548 for the 5 Hz, 4 Hz and 3 Hz cases, respectively, which align very closely to those estimated from the oscillatory motion. This confirms the consistency between positional (Fig. 7) and velocity (Fig. 8) data and that, in general, the velocity of the agitator tube is well predicted by its period of oscillation. It is also noted that these local Reynolds numbers are all within the transitional regime, highlighting the mixing limitations of this system. Nonetheless, previous simulations of a similar ATR system by Derksen [38] predicted rapid micro-mixing for a 5 Hz oscillation case, although experiments by Miller et al. [59], indicated the ATR performed relatively poorly as a liquid-liquid extractor, for which application of high levels of turbulence are required to generate fine droplets.

It is interesting to revisit the observation that, as shown in Fig. 8, the velocities are not perfectly sinusoidal. In fact, there is an inflection within each cycle as the velocities pass zero (which occurs as the agitator is at the extremity of displacement and begins to move in the opposite direction). This inflection is most notable in the experimental data and is also present in the numerical results, and is consistent with previous simulations with a solid agitator bar [37]. The inflection is due to a phase lag between the inner and outer tubes that occurs as the outer (*i.e.* driven) tube changes direction, and is clearest in the angular velocity of the inner tube, the motion of which is mediated by the fluid. The correlation of this inflection in the angular velocity data between experiments and simulations (where the velocities cross zero) is very close, where most of the difference between experimental and numerical results is observed is at the extremities of motion, rather than at the mid-point inflection.

Additionally, it is noted that the peak angular velocity data is slightly over-predicted in all cases by the simulations. This discrepancy may be due to an additional elastic force that the agitator receives from the mechanical knocking at the extremes of its motion, evident in the horizontal *versus* vertical location data (Fig. 7(c)) causing angular movement additional to that predicted purely from the agitator rolling motion. Indeed, in both position (Fig. 7) and velocity (Fig. 8) plots, the experimental data show more structure in general, likely due to mechanical flexing of the physical agitator which is difficult to eliminate in any real system. Additionally, it is noted that the agitator bar itself is slightly smaller than the outer tube, and thus there may be some further slight axial movement and realignment that is not accounted for in the

simulations. The deviation from pure sinusoidal motion observed clearly in the two example runs of the outer tube (Fig. 5(a) and (b)) is also seen in the positional data for the agitator, particularly for Case 3 (iii). It is also present in the velocity data in Fig. 8 (most notably for Case 3, which is to be expected as the velocity data are derived from the positional data). However, despite these differences, in general, the physical and simulation results are in excellent agreement, providing strong validation for the numerical model of the agitator motion and the experimental system used to measure it.

Given the convincing validation of the LBM model, more detailed investigations of the agitator impact on the resulting fluid velocities were made *via* simulation. An example of the agitator motion at an agitation frequency of about 3 Hz (Case 3) is presented in Fig. 9, which shows the velocity field in a 2D slice within the reactor tube, for three relative positions of the agitator (shown in white) – (a) left, (b) middle and (c) right (noting the colour scale is in m/s). It is clear, firstly, that the fluid is well coupled to the agitator, as, in general, regions of high fluid velocities are within the same regions as the agitator (magnitude of the order of 40 mm/s, or 0.4 m/s as given). Most notable, however, is that the agitator motion generates fluid wakes within the perforated holes, creating small regions of high fluctuating velocities, where shear mixing will be enhanced. These regions are clearly seen to trail the agitator as fluid is pushed through the perforations (they only appear to be in front of the agitator in Fig. 9(a) due to phase lag) and, consistent with previous simulations by Derksen [38], are expected to cause higher levels of micro-mixing, despite relatively low peak Reynolds numbers.

3.3. Effect of suspended solid particles on fluid and agitator dynamics

Many applications of the ATR rely on the use of complex multiphase mixtures containing a solid phase, *e.g.* for catalysis [24] or dye removal [28]. For this reason, the influence of palladium-coated carbon particles (as described in the methodology) on agitator motion was investigated experimentally. In particular, the effect of suspended solids on the dynamics of the flow was studied, specifically (a) the rotational motion of the inner agitator tube, using the image analysis method, and (b) the transverse (*i.e.* radial) flow velocity within the outer tube, using the acoustic measurement system [51].

The results for the rotational motion of the agitator tube are presented in Fig. 10, which shows the phase-averaged angular velocity of the agitator tube in two runs at the same nominal driving frequency (both $f \approx 3$ Hz), and similar amplitudes ($a = 11.2$ and 12.6 mm), with and without the carbon catalyst particles at a mass concentration of $\phi_m = 0.1$ wt%. It is clear that the presence of suspended solids appeared to have a negligible effect on the motion of the agitator. It was not possible to obtain video data at higher concentrations: the video analysis procedure requires that the orange-red tracking points attached to the end of the agitator tube be visible through a viewing window, which was not the case at $\phi_m = 0.5$ and 1% by weight, as the suspension was too opaque.

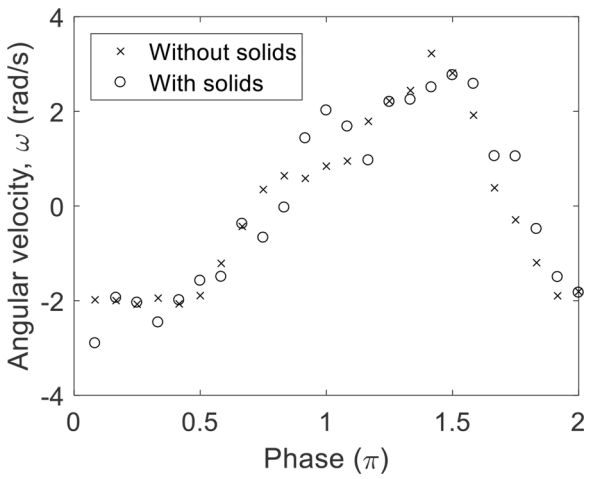

Fig. 10. Comparison of phase-averaged angular velocity of agitator tube with and without carbon particles at $\phi_m = 0.1$ wt%, $f \approx 3$ Hz, from high-speed video analysis, with 24 phase slices shown.

The effect of suspended solids on the fluid velocity field was investigated at three nominal solids concentrations – $\phi_m = 0$, 0.1 and 1 wt% – for Case 1 ($f \approx 5$ Hz) using the UVP, which allowed non-intrusive measurements through visually opaque systems. Phase-averaged mean horizontal fluid velocity profiles along the horizontal inner diameter of the outer (*i.e.* driven) tube are shown in Fig. 11. The velocity profiles are very similar to each other, and the solids loading therefore appears to have little effect on the fluid motion in the reactor, at least for the concentrations considered.

The phases of motion shown in Fig. 11 should be understood as follows. The UVP system measures the velocity field *via* the Doppler effect such that a negative velocity indicates the acoustic scatterers are moving away from the probe, and a positive velocity indicates they are moving towards it. Phase 0 corresponds to the inner tube being closest to the probe, *i.e.* at its right-most point from the perspective of the experimental observations (see Fig. 1). In the following phase, Phase 1, the velocity field becomes negative. Similarly, Phase 4 corresponds to the inner tube at its left-most position, and the velocity field becomes positive in Phase 5.

Therefore, the agitator velocity becomes zero at the extremities of motion (Phases 0 and 4) and fluid velocities reach a maximum as the agitator passes its central position in either direction (Phases 2 and 6) such that $x_A = 0$. The two velocity peaks observed in the data in all three cases in Fig. 11 are at the position of the agitator itself (similar to the simulation profiles in Fig. 9). The fact that the fluid velocities decay slowly away from these peaks implies a degree of fluid coupling to the agitator and illustrates the influence of wakes caused by the perforations, as is also evident in the simulations.

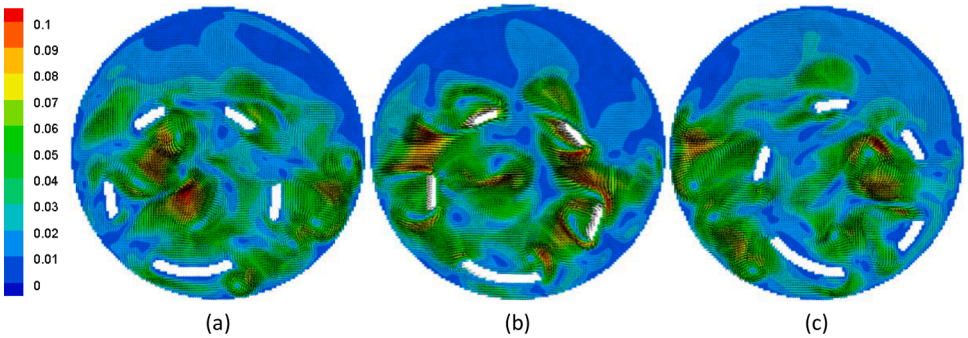

Fig. 9. Simulation of ATR fluid velocity as a 2D slice, in reference frame of outer (*i.e.* mechanically driven) tube, in which inner agitator is (a) to left, (b) at middle and (c) to right of extremities of its movement. Amplitude $a = 11.2$ mm, frequency $f = 3.13$ Hz (Case 3). Velocity scale is m/s.

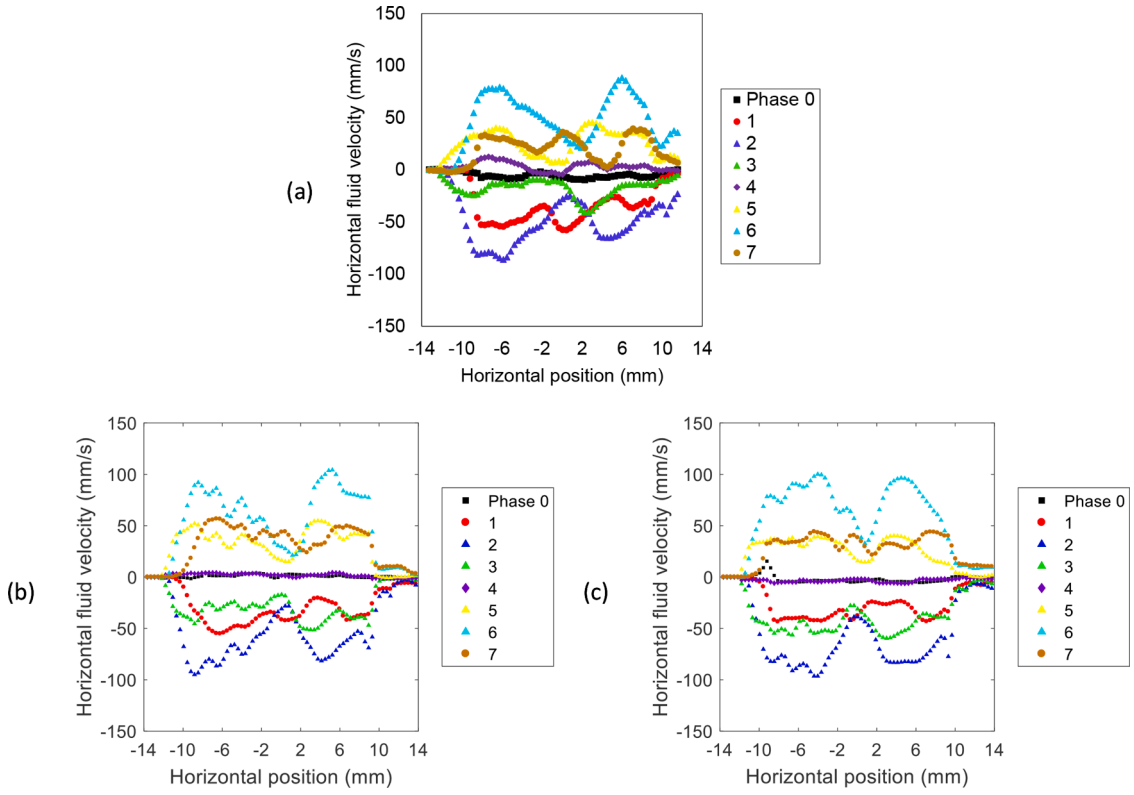

Fig. 11. Phase-resolved mean fluid velocity in horizontal (radial) direction sampled along horizontal line, Case 1 ($f \approx 5$ Hz). Experimental results *via* acoustic Doppler at solids loadings (a) no solids, (b) 0.1 wt% and (c) 1 wt%. Eight phase slices shown, for clear visualisation.

3.4. Power consumption

The power input per unit volume, P_V, by the agitator is of fundamental importance when designing and assessing multiphase processes and is a crucial parameter in reactor design. It affects heat and mass-transfer processes, as well as mixing and circulation time, and so accurate estimation of power input is required for the scale-up, operation and optimisation of reactor designs. For the ATR system studied here, all power input is from the agitator tube and P_V can be calculated as follows:

$$P_v = \frac{-\sum(\mathbf{F}\cdot\mathbf{U} + \mathbf{T}\cdot\boldsymbol{\omega})}{V}, \tag{6}$$

where **F** is the translational force, **U** is the translational velocity, **T** is the torque experienced by the agitator, **ω** is the angular velocity, and V is the reactor tube volume. Within the numerical model, these forces and torques were computed using the immersed boundary approach, as summarised in Section 2.3 and described previously [37].

The power consumption of the agitator tube per unit volume, calculated using the numerical simulation to find the parameters in Eq. (6), is presented in a phase-averaged form in Fig. 12(a), for each of the three sets of operating conditions chosen as case studies (see Table 3). The power consumption shows a well-behaved periodicity, and it is important to note that the agitator tube does not always impart energy into the fluid; in fact, as is clear from Fig. 12(a) that P_V may become slightly negative – and the fluid therefore does work on the agitator, and not *vice versa* – at some phase positions, due to the reversal of the direction of motion of the agitator.

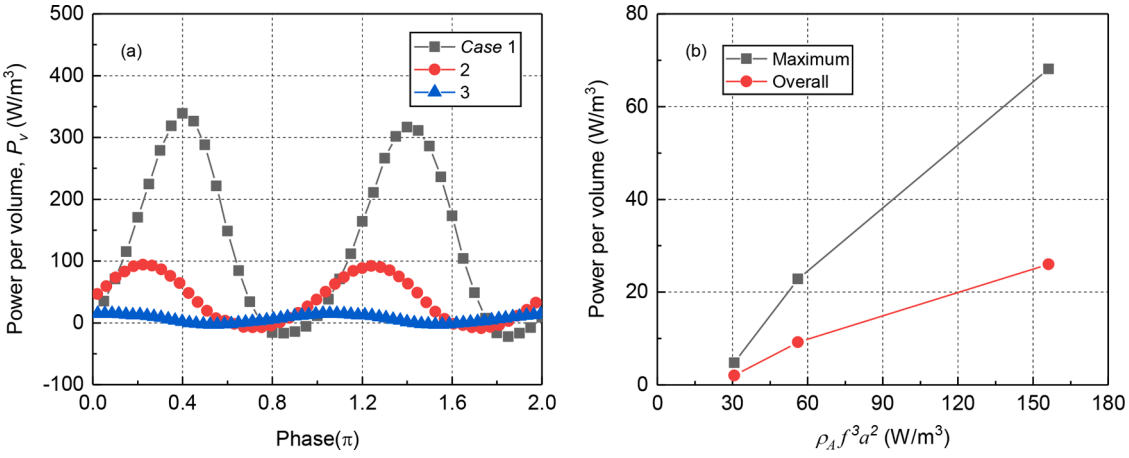

Fig. 12. (a) Power consumption per unit volume *versus* oscillation under different agitation conditions, (b) averaged and maximum power dissipation (P_V *versus* $\rho_l f^3 a^2$).

It is also possible to derive P_V phenomenologically. The kinetic energy of the agitator tube at its maximum velocity, $U_{\max}$, is:

$$E = \frac{1}{2} M_A U_{\max}^2, \tag{7}$$

where M_A is the mass of the agitator and $U_{\max} \propto fa$ ($U_{max} = 2\pi fa$) where again, a, indicates the agitator amplitude as shown in column 3 of Fig. 7. It is assumed that a fraction of the kinetic energy is dissipated as turbulence kinetic energy. As a result of the motion of the agitator on each traversal of the agitator through the reactor tube, the dissipation rate, P_A, is:

$$P_A \propto M_A U_{\max}^2 f = M_A f^3 a^2 \tag{8}$$

If the agitator has a length H, a diameter D_A, a wall thickness βD_A (expressed as a fraction of the diameter) and the area fraction of holes in the surface is ε, then $M_A = (1-\varepsilon)\beta\rho_A \pi D_A^2 H$, and Eq. (8) reduces to:

$$P_A \propto \rho_A f^3 a^2 D_A^2 H \tag{9}$$

If the ratio of the agitator diameter to reactor tube diameter is constant, the reactor tube volume, V_R, is proportional to $D_A{}^2H$, so the power per unit volume, P_V, can be calculated from Eq. (10) as follows:

$$P_v = \frac{P_A}{V_R} \propto \rho_A f^3 a^2 \tag{10}$$

It follows that the relationship between P_V and $\rho_A f^3 a^2$ should be linear, and it is noted that the result of this analysis is similar to that for agitators in batch vessels [60-62], in which $P_V \approx \rho_L N^3 D^2$, and N is the agitation rate (s^{-1}). The overall power dissipation per unit volume is the time-averaged power in the system, as follows:

$$\overline{P_v} = \frac{f}{V_R} \int_0^{1/f} P_v(t)\,dt \tag{11}$$

The system's power input based on the maximum observed power (Eq. (10) at max peak power in Fig. 12(a)) and the phase averaged power (Eq. (11)) are compared in Fig. 12(b). The maximum P_V is approximately twice the averaged value, $\overline{P_v}$, and above a critical value, P_V does indeed vary approximately linearly with $\rho_A f^3 a^2$, as postulated in the phenomenological model. However, it is also evident that there is a critical value of $\rho_A f^3 a^2 \approx 30$, below which there is no significant turbulence energy generation by the agitator tube due the effect of fluid inertia within the system.

In typical batch vessels, the performance of an agitator is characterised by a power number, Po, which represents the agitator's drag coefficient under turbulent conditions. When agitating at lower values of the Reynolds number, characteristic mixing power numbers typically increase as given in Eq. (12), where k is a constant and the linear relationship is derived from log-log scale plots [62]:

$$Po(Re) = \frac{k}{Re} + Po_{Re=\infty} \tag{12}$$

The power number in the case of the ATR may be defined as in Eq. (13), while the Reynolds number is defined, as previously given, in Eq. (5).

$$Po = \frac{P_A}{\rho_A f^3 a^2 D_A^2 H} \tag{13}$$

Fig. 13 presents the calculated power number *versus* Reynolds number for the three simulated test cases, and it is clear that the behaviour of a mobile, disconnected agitator tube at $Re > 1000$ is essentially constant, and Eq. (12) applies. It is noted that the slight discrepancy in Re values to those reported earlier are due to the use of the simulated oscillation amplitudes (a) rather than the experimental values in the earlier section, where differences are mostly evident only in Case 3. The observed power number is similar to that of a single blade

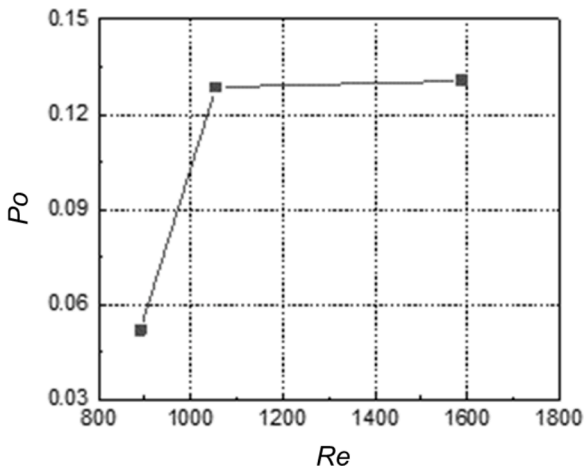

Fig. 13. Relationship between power number (Po) and Reynolds number (Re) for three test cases.

of a curved-blade axial flow type impeller, for which $Po \approx 0.1$–0.15 per blade [63,64], but varies significantly from a shaft-driven agitator in that, at low Re, the power number drops to very low levels, rather than following Eq. (12). This discrepancy arises because, at low Re in agitated vessels, the viscous forces dominate, and the power number increases with $1/Re$. For the ATR, significant viscous forces are present at low Re, but unlike motor driven impellers, this results in a significant reduction of movement of the agitation tube relative to the wall of the vessel. As there is no external force on the agitator tube, it comes to a virtual stop, with no power being transferred to the fluid, reducing P_v essentially to zero at low Re. Collectively, this work suggests a significant drop-off in mixing performance at low oscillation frequencies, whereas optimal operating conditions occur in a narrow region from 4 to 5 Hz.

4. Conclusions

An agitated tubular reactor (ATR), designed and built by AM Technology, underwent extensive experimental and numerical characterisation, the goal being to understand the dynamics of the internal agitator and its effect on fluid mixing, as well as to validate a numerical model. The motion of the ATR was varied over a range of parameters (specifically, the frequency of oscillation and the applied pneumatic pressure used to drive the bulk displacement of the reactor) that were selected in order to represent real operating conditions. The investigations were intended to provide future users with all possible combinations of parameters, and to provide assurance to operators on the optimal operating conditions.

To characterise the system experimentally, non-invasive high-speed image analysis, as well laser and ultrasonic velocity and backscatter devices, were used over a range of agitation frequencies (f = 2–6 Hz overall, $f \approx$ 3–5 Hz in test cases) to measure the motion of the outer tube and inner agitator. Experimental results were compared to computational fluid dynamic simulations of the ATR under the same conditions, using a powerful LBM framework. Overall, very good agreement was found between experiment and simulation in terms of agitator dynamics within the measurement domain, both in terms of agitator displacement and translational and rotational velocities, demonstrating that the numerical model very faithfully predicted the behaviour of the physical system. However, at the lowest oscillation frequency, there appeared to be non-sinusoidal mechanical motion caused by knocking and inertia in the physical system that limited movement more than predicted by the numerical results. Also, for the highest agitation frequency, there was some evidence that the agitator bar lost direct contact with the reactor tube at the extremities of motion, due to mechanical flexibility in the platform mounting. Despite these observations, the numerical model

was determined to be well validated and was used to probe the fluid dynamics, highlighting the formation of high-shear zones as the fluid passes through perforations in the agitator tube. Ultrasonic profiling also demonstrated that horizontal fluid velocities were closely coupled to the agitator in the vicinity of the agitator tube bar. The presence of solid particles (at 0.1 wt%) on the rotational dynamics of the agitator tube was investigated and found to have no discernible effect. In addition, the mean velocity field was not found to be affected by the presence of solid particles up to industrially realistic concentrations (0.1 and 1 wt%, by comparison to zero solids loading).

The numerical model was also used to calculate power dissipation per unit volume. The power dissipation was found to rapidly increase with the frequency of motion and was limited by the device's maximum operating frequency. A driving frequency of $f = 5$ Hz is recommended on the basis of mixing efficiency and enhanced solids dispersion that are likely to be present in multiphase mixtures that the reactor was designed to process. A theoretical power number was derived, using a phenomenological model, and calculated using results from the numerical model. There was found to be a critical frequency below which the power input by the agitator tube is zero; above the critical frequency the power input per unit volume was found to vary as f^3a^2.

Overall, ATRs have the potential to address a range of applications in which complex suspensions and flows require intense agitation without recourse to large apparatus. Although ATRs cannot satisfy the extreme operating conditions of small-tube ceramic reactors in terms of heat transfer rates or spinning disc reactors in terms of mass transfer rates, they can be run fully continuously (in practice, by using multiple reaction volumes in series or parallel), and the results presented here demonstrate that ATR systems, although dynamically complex, can (a) be modelled very accurately numerically, and (b) be well understood using standard phenomenological analysis, which allows direct comparison with other process technologies. Both the experimental techniques – a combination of laser, optical and acoustic – and the numerical model are highly sophisticated and can be applied to other flow geometries for direct comparison to the ATR. This study represents a description of a suite of methods for investigation of flows in complex or novel geometries – including systems with moving parts that are not accessible by other techniques – and are not limited to the flows and geometries present in ATRs.

CRediT authorship contribution statement

Hugh P. Rice: Conceptualization, Data curation, Formal analysis, Investigation, Methodology, Software, Validation, Visualization, Writing – original draft, Writing – review & editing. **Yi He:** Conceptualization, Data curation, Formal analysis, Investigation, Methodology, Software, Validation, Visualization, Writing – original draft, Writing – review & editing. **Frans L. Muller:** Conceptualization, Funding acquisition, Project administration, Resources. **Andrew E. Bayly:** Conceptualization, Project administration, Writing – original draft. **Robert Ashe:** Conceptualization, Funding acquisition, Project administration, Resources. **Andrew Karras:** Conceptualization, Project administration, Writing – original draft. **Ali Hassanpour:** Conceptualization, Funding acquisition, Writing – original draft. **Richard A. Bourne:** Conceptualization, Funding acquisition, Project administration, Writing – original draft. **Michael Fairweather:** Conceptualization, Funding acquisition, Project administration, Supervision, Writing – original draft, Writing – review & editing. **Timothy N. Hunter:** Conceptualization, Funding acquisition, Methodology, Project administration, Resources, Supervision, Writing – original draft, Writing – review & editing.

Declaration of Competing Interest

The authors declare that they have no known competing financial interests or personal relationships that could have appeared to influence the work reported in this paper.

Data for reference

Data will be made available on request.

Acknowledgments

The authors would like to thank the European Commission for supporting this work as part of the research project "*Intensified by Design,* for the intensification of processes involving solids handling (IbD)", under the 2020 SPIRE programme (SPIRE-08-2015-680565). The authors also thank Peter Dawson, Chris Bulman and Bob Harris for their technical assistance. TH and HR also acknowledge additional support from the Engineering & Physical Sciences Research Council (EPSRC) UK, through an Impact Acceleration Account (EP/R511717/1).

References

[1] I.R. Baxendale, The integration of flow reactors into synthetic organic chemistry, J. Chem. Technol. Biotechnol. 88 (2013) 519–552.
[2] D.L. Browne, M. Baumann, B.H. Harji, I.R. Baxendale, S.V. Ley, A new enabling technology for convenient laboratory scale continuous flow processing at low temperatures, Org. Lett. 13 (2011) 3312–3315.
[3] N. Holmes, G.R. Akien, R.J.D. Savage, C. Stanetty, I.R. Baxendale, A.J. Blacker, B. A. Taylor, R.L. Woodward, R.E. Meadows, R.A. Bourne, Online quantitative mass spectrometry for the rapid adaptive optimisation of automated flow reactors, React. Chem. Eng. 1 (2016) 96–100.
[4] L. Malet-Sanz, F. Susanne, Continuous flow synthesis. A pharma perspective, J. Med. Chem. 55 (2012) 4062–4098.
[5] J.C. Pastre, D.L. Browne, S.V. Ley, Flow chemistry syntheses of natural products, Chem. Soc. Rev. 42 (2013) 8849–8869.
[6] L.J. Martin, A.L. Marzinzik, S.V. Ley, I.R. Baxendale, Safe and reliable synthesis of diazoketones and quinoxalines in a continuous flow reactor, Org. Lett. 13 (2011) 320–323.
[7] J.A. Newby, D.W. Blaylock, P.M. Witt, J.C. Pastre, M.K. Zacharova, S.V. Ley, D. L. Browne, Design and application of a low-temperature continuous flow chemistry platform, Org. Process Res. Dev. 18 (2014) 1211–1220.
[8] H. Wang, A. Mustaffar, A.N. Phan, V. Zivkovic, D. Reay, R. Law, K. Boodhoo, A review of process intensification applied to solids handling, Chem. Eng. Proc. 118 (2017) 78–107.
[9] P. Pollak, A. Badrot, R. Dach, API Manufacturing: Facts and Fiction, Contract Pharma, 01.23.12, Rodman Media, New Jersey, 2012.
[10] X. Ni, J.C. Johnstone, K.C. Symes, B.D. Grey, D.C. Bennett, Suspension polymerization of acrylamide in an oscillatory baffled reactor: from drops to particles, AIChE J. 47 (2001) 1746–1757.
[11] A.P. Harvey, M.R. Mackley, T. Seliger, Process intensification of biodiesel production using a continuous oscillatory flow reactor, J. Chem. Technol. Biotechnol. 78 (2003) 338–341.
[12] T. Coward, H. Tribe, A.P. Harvey, Opportunities for process intensification in the UK water industry: a review, J. Water Process. Eng. 21 (2018) 116–126.
[13] F. Ghadyanlou, A. Azari, A. Vatani, A review of modeling rotating packed beds and improving their parameters: gas–liquid contact, Sustainability 13 (2021) 8046.
[14] S. Sana, V. Zivkovic, K. Boodhoo, Shear-thinning effect of the spinning disc mixer on starch nanoparticle precipitation, Processes 8 (2020) 1622.
[15] F. Visscher, J. van der Schaaf, T.A. Nijhuis, J.C. Schouten, Rotating reactors – a review, Chem. Eng. Res. Des. 91 (2013) 1923–1940.
[16] S. Haase, P. Tolvanen, V. Russo, Process intensification in chemical reaction engineering, Processes 10 (2022) 99.
[17] A. Ghanem, T. Lemenand, D. Della Valle, H. Peerhossaini, Static mixers: mechanisms, applications, and characterization methods – a review, Chem. Eng. Res. Des. 92 (2014) 205–228.
[18] P. Bianchi, J.D. Williams, C.O. Kappe, Oscillatory flow reactors for synthetic chemistry applications, J. Flow Chem. 10 (2020) 475–490.
[19] M. Avila, B. Kawas, D.F. Fletcher, M. Poux, C. Xuereb, J. Aubin, Design, performance characterization and applications of continuous oscillatory baffled reactors, Chem. Eng. Proc. (2021), 108718.
[20] A. Laybourn, A.M. López-Fernández, I. Thomas-Hillman, J. Katrib, W. Lewis, C. Dodds, A.P. Harvey, S.W. Kingman, Combining continuous flow oscillatory baffled reactors and microwave heating: process intensification and accelerated synthesis of metal-organic frameworks, Chem. Eng. J. 356 (2019) 170–177.
[21] M. Wernik, G. Sipos, B. Buchholcz, F. Darvas, Z. Novák, S.B. Ötvös, C.O. Kappe, Continuous flow heterogeneous catalytic reductive aminations under aqueous micellar conditions enabled by an oscillatory plug flow reactor, Green Chem. 23 (2021) 5625–5632.
[22] C. Rosso, S. Gisbertz, J.D. Williams, H.P.L. Gemoets, W. Debrouwer, B. Pieber, C. O. Kappe, An oscillatory plug flow photoreactor facilitates semi-heterogeneous dual nickel/carbon nitride photocatalytic C–N couplings, React. Chem. Eng. 5 (2020) 597–604.
[23] J.R. McDonough, S. Murta, R. Law, A.P. Harvey, Oscillatory fluid motion unlocks plug flow operation in helical tube reactors at lower Reynolds numbers (Re $\leq$ 10), Chem. Eng. J. 358 (2019) 643–657.

[24] G. Gasparini, I. Archer, E. Jones, R. Ashe, Scaling up biocatalysis reactions in flow reactors, Org. Process Res. Dev. 16 (2012) 1013–1016.
[25] D.L. Browne, B.J. Deadman, R. Ashe, I.R. Baxendale, S.V. Ley, Continuous flow processing of slurries: evaluation of an agitated cell reactor, Org. Process Res. Dev. 15 (2011) 693–697.
[26] P. Filipponi, A. Gioiello, I.R. Baxendale, Controlled flow precipitation as a valuable tool for synthesis, Org. Process Res. Dev. 20 (2016) 371–375.
[27] A.T. Pedersen, T.M. de Carvalho, E. Sutherland, G. Rehn, R. Ashe, J.M. Woodley, Characterization of a continuous agitated cell reactor for oxygen dependent biocatalysis, Biotechnol. Bioeng. 114 (2017) 1222–1230.
[28] A.S. Tonge, D. Harbottle, S. Casarin, M. Zervaki, C. Careme, T.N. Hunter, Coagulated mineral adsorbents for dye removal, and their process intensification using an agitated tubular reactor (ATR), ChemEngineering 5 (2021) 35.
[29] H. Yao, L. Wan, X. Zhao, Y. Guo, J. Zhou, X. Bo, Y. Mao, Z. Xin, Effective phosphorylation of 2,2′-methylene-bis(4,6-di-tert-butyl) phenol in continuous flow reactors, Org. Process Res. Dev. 25 (2021) 2060–2070.
[30] M. Jiang, M. Liu, H. Huang, F. Chen, Fully continuous flow synthesis of 5-(aminomethyl)-2-methylpyrimidin-4-amine: a key intermediate of vitamin B1, Org. Process Res. Dev. 25 (2021) 2331–2337.
[31] A. Karadeolian, D. Patel, P. Bodhuri, G. Weeratunga, B. Gorin, Continuous flow process for reductive deoxygenation of ω-chloroketone in the synthesis of vilazodone, Org. Process Res. Dev. 22 (2018) 1022–1028.
[32] M. Baumann, I.R. Baxendale, P. Filipponi, T. Hu, Sustainable flow synthesis of a versatile cyclopentenone building block, Org. Process Res. Dev. 21 (2017) 2052–2059.
[33] L. Chuzeville, F. Boury, D. Duday, R. Anand, E. Moretto, J.-.S. Thomann, Eco-friendly processes for the synthesis of amorphous calcium carbonate nanoparticles in ethanol and their stabilisation in aqueous media, Green Chem. 24 (2022) 1270–1284.
[34] E. Jones, K. McClean, S. Housden, G. Gasparini, I. Archer, Biocatalytic oxidase: batch to continuous, Chem. Eng. Res. Des. 90 (2012) 726–731.
[35] M.Y. Prajitno, M. Taufiqurrakhman, D. Harbottle, T.N. Hunter, Kinetic studies of Cs + and Sr2+ ion exchange using clinoptilolite in static columns and an agitated tubular reactor (ATR), ChemEngineering 5 (2021) 9.
[36] J. Miller, Solvent Extraction and Mass Transfer Assessment in Novel Extraction Technologies,, Ph.D. thesis,, School of Chemical and Process Engineering, University of Leeds, 2021.
[37] Y. He, A.E. Bayly, A. Hassanpour, M. Fairweather, F. Muller, Flow behaviour of an agitated tubular reactor using a novel dynamic mesh based CFD model, Chem. Eng. Sci. 212 (2020), 115333.
[38] J.J. Derksen, Mixing in an agitated tubular reactor, Can. J. Chem. Eng. 97 (2019) 523–527.
[39] P. Mavros, Flow visualization in stirred vessels: a review of experimental techniques, Chem. Eng. Res. Des. 79 (2001) 113–127.
[40] H. Wu, G.K. Patterson, Laser-Doppler measurements of turbulent-flow parameters in a stirred mixer, Chem. Eng. Sci. 44 (1989) 2207–2221.
[41] M. Afkhami, A. Hassanpour, M. Fairweather, D.O. Njobuenwu, Fully coupled LES-DEM of particle interaction and agglomeration in a turbulent channel flow, Comput. Chem. Eng. 78 (2015) 24–38.
[42] C. Pan, J. Min, X. Liu, Z. Gao, Investigation of fluid flow in a dual Rushton impeller stirred tank using particle image velocimetry, Chin. J. Chem. Eng. 16 (2008) 693–699.
[43] R. Zadghaffari, J.S. Moghaddas, J. Revstedt, A mixing study in a double-Rushton stirred tank, Comput. Chem. Eng. 33 (2009) 1240–1246.
[44] H.D. Cheng, X.H. Jiang, Y. Sun, J. Wang, Color image segmentation: advances and prospects, Pattern Recognit. 34 (2001) 2259–2281.
[45] A.E. Hay, J.Y. Sheng, Vertical profiles of suspended sand concentration and size from multifrequency acoustic backscatter, J. Geophys. Res. Oceans 97 (1992) 15661–15677.
[46] P.D. Thorne, D.M. Hanes, A review of acoustic measurement of small-scale sediment processes, Cont. Shelf Res. 22 (2002) 603–632.
[47] T.N. Hunter, J. Peakall, T.J. Unsworth, M.H. Acun, G. Keevil, H. Rice, S. Biggs, The influence of system scale on impinging jet sediment erosion: observed using novel and standard measurement techniques, Chem. Eng. Res. Des. 91 (2013) 722–734.
[48] H.P. Rice, M. Fairweather, T.N. Hunter, J. Peakall, S.R. Biggs, The influence of relative fluid depth on initial bedform dynamics in closed, horizontal pipe flow, Int. J. Multiph. Flow 93 (2017) 1–16.
[49] H.P. Rice, M. Fairweather, J. Peakall, T.N. Hunter, B. Mahmoud, S.R. Biggs, Constraints on the functional form of the critical deposition velocity in solid-liquid pipe flow at low solid volume fractions, Chem. Eng. Sci. 126 (2015) 759–770.
[50] H.P. Rice, J. Peakall, M. Fairweather, T.N. Hunter, Extending estimation of the critical deposition velocity in solid–liquid pipe flow to ideal and non-ideal particles at low and intermediate solid volume fractions, Chem. Eng. Sci. 211 (2020), 115308.
[51] H.P. Rice, J.L. Pilgrim, M. Fairweather, J. Peakall, D. Harbottle, T.N. Hunter, Extending acoustic in-line pipe rheometry and friction factor modeling to low-Reynolds-number, non-Newtonian slurries, AIChE J. 66 (2020) e16268.
[52] Y. Takeda, Ultrasonic Doppler method for velocity profile measurement in fluid dynamics and fluid engineering, Exp. Fluids 26 (1999) 177–178.
[53] T. Wunderlich, P.O. Brunn, Ultrasound pulse Doppler method as a viscometer for process monitoring, Flow Meas. Instrum. 10 (1999) 201–205.
[54] M.J.W. Povey, Ultrasonic Techniques for Fluids Characterization, Academic Press, San Diego, 1997.
[55] S.J. Orfanidis, Introduction to Signal Processing, Prentice Hall, New Jersey, 1996.
[56] H.P. Rice, Transport and Deposition Behaviour of Model Slurries in Closed Pipe Flow,, Ph.D. thesis,, School of Process, Environmental and Materials Engineering, University of Leeds, 2013.
[57] J. Derksen, H.E.A. Van den Akker, Large eddy simulations on the flow driven by a Rushton turbine, AIChE J. 45 (1999) 209–221.
[58] A. Ten Cate, C.H. Nieuwstad, J.J. Derksen, H.E.A. Van den Akker, Particle imaging velocimetry experiments and lattice-Boltzmann simulations on a single sphere settling under gravity, Phys. Fluids 14 (2002) 4012–4025.
[59] J. Miller, B. Hanson, F. Muller, Design optimisation for solvent extraction in a modified agitated tube reactor –19400, in: WM2019: Waste Management Conference, Phoenix, USA, 2019.
[60] A.W. Nienow, M.F. Edwards, N. Harnby. Mixing in the Process Industries, 1st ed., Butterworth-Heinemann, Oxford, 1997.
[61] J.Y. Oldshue, Fluid Mixing Technology, McGraw-Hill, New York, 1983.
[62] E.L. Paul, V.A. Atiemo-Obeng, S.M. Kresta, Handbook of Industrial mixing: Science and Practice, 1, John Wiley & Sons, Hoboken, 2004.
[63] N.J. Fentiman, N. St.Hill, K.C. Lee, G.R. Paul, M. Yianneskis, A novel profiled blade impeller for homogenization of miscible liquids in stirred vessels, Chem. Eng. Res. Des. 76 (1998) 835–842.
[64] M. Cooke, Design of Mechanically Agitated Contactors Or Reactors With "attitude, Ph.D. thesis, School of Chemical Engineering and Analytical Science, University of Manchester, 2005.